Illustration of the role of saddle-point and molecular-type ionization mechanisms in atomic collisions

Clara Illescas,[1] I. Rabadán,[2] A. Riera[1]
[1]*Departamento de Química, C-IX, Universidad Autónoma de Madrid, Cantoblanco, E-28049 Madrid, Spain*
[2]*Department of Physics and Astronomy, University College, London, United Kingdom*
(Received 9 June 1997)

We complete a previous description of classical ionization in $He^{2+}+H$ collisions, extending the energy range of the illustrations and using as initial conditions either a microcanonical distribution or a hydrogenic one that produces better cross sections near threshold. We call those ionizing electrons that are bound in a frame where the nuclear motion is suppressed molecular-type electrons. We illustrate the evolution of these electrons in phase space, and show that it may properly be called saddle-point ionization at low nuclear velocities, while they give rise at high energies to the standard direct ionization process. [S1050-2947(98)01603-5]

PACS number(s): 34.10.+x

I. INTRODUCTION

In the treatment of atomic collisions at intermediate energies, detailed information on the characteristics and evolution of the ionizing densities is required [1] in order to improve upon the quality of close-coupling basis sets. To obtain this information, in Ref. [2] we studied the main properties of electronic distributions obtained from a classical trajectory Monte Carlo (CTMC) treatment for $He^{2+}+H$ collisions. The results of our analysis were then employed in a preliminary work [3] to generate new close-coupling bases, for the $He^{2+}+H$ system. This system was shown in Refs. [1, 4] to be a good benchmark for $X^{q+}+H$ collisions.

An interesting feature of our previous study concerned the so-called saddle-point ionization (SPI)—a topic introduced by Olson [5] that has given rise to many works and some controversies (see, e.g., Refs. [2,6]). We found, on the one hand, that the saddle part of the nuclear potential indeed plays a crucial role at nuclear velocities $v<1$ a.u. but not at higher energies; and, on the other hand, that the corresponding mechanism at high energies is the standard direct ionization process [7–9] yielding soft electrons. For $He^{2+}+H$ collisions, the present work illustrates these findings, which were only briefly mentioned in Ref. [2].

With regards to the low-energy results, we shall focus on the properties of the electronic distribution, and analyze whether the characteristics of the ionization mechanism are such that it can properly be called SPI. We shall also study to what extent our conclusions on this point depend upon the use of the standard initial microcanonical distribution in the CTMC treatment. This is a pertinent question, since the corresponding initial spatial $H(1s)$ density significantly differs from the quantum mechanical one [10–12], and a consequence of this unphysical feature is that standard CTMC calculations yield [13,2] a shift of the threshold region. Consequently, the ionization cross section calculated with the usual CTMC method is inaccurate precisely in the energy range where the SPI mechanism was found to be operative. Then, in order to answer the question, we shall also present results, at low nuclear velocities v, from (nonstandard) CTMC calculations carried out with an improved initial distribution [14] that reproduces both spatial and momentum densities of $H(1s)$ to a good approximation.

In the present work we shall also illustrate the evolution of the SPI mechanism as the impact energy increases. In particular, the correspondence between low- and higher-v electron distributions will be established by developing an original idea of Bandarage and Parson [13], who studied the time evolution of electron trajectories in a quasistatic molecular frame in which the nuclear motion is suppressed (as in the Born-Oppenheimer approximation of quantal treatments). We shall call *molecular type* those ionizing electrons that are bound in this clamped-nuclei frame. Then, a separate study of molecular-type and nonmolecular ionizing electrons provides useful information on the properties of the ionizing distributions at a given nuclear velocity v, and on the variation of the mechanism as this velocity is changed. Furthermore, and as reasoned in Refs. [2,3], the properties and time dependence of the molecular-type distribution bear a relation to molecular pictures of ionization, such as provided by the hidden crossing model [15,16], and to the relay-race mechanism described in Refs. [4,1] for close-coupling treatments.

Our paper is organized as follows. Section II A presents a summary of the methods; Sec. II B is devoted to defining molecular-type and nonmolecular electronic distributions; and Sec. II C describes the tools employed in our illustrations, which are arrow diagrams simultaneously displaying electronic positions and momenta, and longitudinal momentum densities. Section III A presents the ionization cross sections, and shows the accuracy achieved by the CTMC treatment when the improved initial condition is employed; Sec. III B contains our illustrations for the standard CTMC calculations, starting from the initial microcanonical distribution; and Sec. III C focuses on the modifications that appear when the treatment is modified to allow for a better representation of the $H(1s)$ radial density. Finally, our conclusions are drawn in Sec. IV.

As a final preliminary remark, and as stressed in Ref. [2], most of the features observed in CTMC illustrations have a known parallel with semi-classical treatments at higher energies, employing either perturbational or close-coupling

techniques—see reviews in Refs. [7–9]. Atomic units are used throughout, except where otherwise indicated.

II. METHOD

A. Distribution functions

As in Ref. [2], to treat $He^{2+}+H(1s)$ collisions we applied the impact-parameter CTMC method. In this method, the internuclear vector $\mathbf{R}$ follows rectilinear trajectories $\mathbf{R}=\mathbf{b}+\mathbf{v}t$, with impact parameter $\mathbf{b}$ and velocity $\mathbf{v}$, while the electronic motion is described through an ensemble of trajectories which are solutions of the Hamilton equations; the treatment is parallel to the semiclassical impact-parameter method usually employed at low and intermediate energies.

As mentioned in Sec. I, our calculations started from either of two initial $H(1s)$ distributions. The first one is the standard microcanonical function, which corresponds to a sharp value of the energy $E=-0.5$ hartree:

$$\rho(\mathbf{r},\mathbf{p};v,b,t\rightarrow-\infty)=\frac{1}{8\pi^3}\,\delta\left(E-\frac{p^2}{2}+\frac{1}{r}\right), \tag{1}$$

where $\mathbf{r}$ and $\mathbf{p}$ are the electron position and momentum vector, respectively, with respect to the target (H) nucleus, which is taken to be at rest, and δ is a delta function. Insertion of Eq. (1) into the Liouville equation shows this distribution to be stable in time, in the absence of the projectile. To generate it, we have employed the procedure of Abrines and Percival [17,18].

Distribution (1) yields an exact initial $H(1s)$ momentum density but a spatial one that is too compact, with a cutoff value $(-E)^{-1}$ (in a.u.). Hence several procedures have been proposed to improve on it. Here we also employed the alternative initial condition proposed in Ref. [14], which is a superposition of eight microcanonical functions:

$$\rho(\mathbf{r},\mathbf{p};v,b,t\rightarrow-\infty)=\sum_{j=1}^{8}\frac{(-2E_j)^{5/2}}{8\pi^3}\,a_j\,\delta\left(E_j-\frac{p^2}{2}+\frac{1}{r}\right). \tag{2}$$

Since the weights a_j are time independent, this function is stable in time, like Eq. (1), in the absence of the projectile. Furthermore, the energies $E_j=-2/j$ hartree $(j=1,\ldots,8)$ were chosen so that the individual cutoff values $(-E_j)^{-1}$ are in an arithmetic progression; and the weights a_j were calculated in Ref. [14] so as to achieve good approximations to the spatial and momentum quantal densities, together with the condition that the mean value $E=\Sigma_j a_j E_j=-0.5$ hartree. CTMC calculations carried out with the initial condition (2) will be called *hydrogenic* in the following sections.

For a given nuclear velocity v, a series of impact parameters b, and starting from either condition (1) or (2), the Hamilton equations were integrated with a variable-step Burlisch-Stoer [19] algorithm. Ionizing trajectories were selected by using, at the end of the time integration ($t=t_{\max}$), the usual energy criterion [20,13]. Along each such trajectory, our numerical integration yielded a test particle discretization for the corresponding ionizing distribution function $\rho^i(\mathbf{r},\mathbf{p};v,b,t)$. Convergence of the results was deemed to be sufficient for our purposes with statistics involving 30 000 trajectories for $v<1$ a.u. and 20 000 trajectories for $v>1$ a.u., together with a value of $t_{\max}=500v^{-1}$ a.u., save for some very loosely bound electrons which were separately investigated [2]. From the asymptotic values of the distribution functions, the ionization cross section σ^i was calculated by addition over all ionizing test particles, and numerical integration over the impact parameter:

$$\sigma^i(v)=2\pi\int_0^\infty db\;b\int d\mathbf{r}\int d\mathbf{p}\;\rho^i(r,\mathbf{p};v,b,t_{\max}) \tag{3}$$

B. Molecular-type ρ^i_- and nonmolecular ρ^i_+ ionizing distributions

As mentioned in Sec. I, it is useful for the present purposes to extend the analysis carried in Ref. [2], regarding the portion of ρ^i which could in principle be reproduced by bound molecular states, and the part which cannot, and therefore requires pseudostates. To obtain these portions, and following an idea of Bandarage and Parson [13], for each set of values $\{\mathbf{r},\mathbf{p},\mathbf{v},\mathbf{R}\}$ we define the electronic molecular energy E_m, that would correspond to the situation where the nuclear motion would be artificially suppressed:

$$E_m(\mathbf{r},\mathbf{p};v,b,t)=\tfrac{1}{2}[\mathbf{p}-f(\mathbf{r},\mathbf{R})\mathbf{v}]^2-\frac{1}{r}-\frac{2}{|\mathbf{r}-\mathbf{R}|}, \tag{4}$$

where the switching function $0\leqslant f(\mathbf{r},\mathbf{R})\leqslant 1$ was introduced originally by Schneiderman and Russek [21], in their definition of a common electron translation factor (CTF) for molecular close-coupling expansions. This function is commonly interpreted [22] as defining a degree of attachment of the electron to one or the other nucleus, so that $f(\mathbf{r},\mathbf{R})\mathbf{v}$ represents an effective drag velocity of the electron due to the nuclear motion. In our calculations, we have chosen the form introduced by Harel and Jouin [23],

$$f(\mathbf{r},\mathbf{R})=\frac{1}{2}\left[1+\alpha^{\alpha/2}\,\frac{\eta}{(\alpha-1+\eta^2)^{\alpha/2}}\right], \tag{5}$$

with $\eta=(r-|\mathbf{r}-\mathbf{R}|)/R$ the spheroidal coordinate, and $\alpha=1.25$ a parameter which was determined in semiclassical molecular calculations for $He^{2+}+H$ collisions using a CTF [24].

Then, assuming an approximate correspondence between classical and close-coupling densities, we have that E_m is the classical analog of the Born-Oppenheimer electronic energy, and may reason that a part of the ionizing cloud with a molecular energy $E_m<0$ could in principle be described by a superposition of bound molecular wave functions, whereas a portion with $E_m>0$ would require the introduction of pseudostates with positive molecular energies. To find these portions, along each ionizing trajectory and at each time t, we distinguished between those ionizing electrons with $E_m<0$ and $E_m>0$, and constructed what we henceforth call molecular-type $\rho^i_-(\mathbf{r},\mathbf{p};v,b,t)$ and nonmolecular $\rho^i_+(\mathbf{r},\mathbf{p};v,b,t)$ ionizing distributions, respectively; notice that at any time we have that the total ionizing distribution function $\rho^i=\rho^i_-+\rho^i_+$ is given by the sum of molecular-type and nonmolecular contributions.

TABLE I. Parameters ϵ and l used in the arrow diagrams of Figs. 5, 6, 7, 8, and 9 (a, b, c, and d) for ionizing electrons lying in the slab $-\epsilon<y<\epsilon$ bohr, with the length of the arrows multiplied by the scaling factor l to improve the clarity of the figure. The coordinates for each arrow are $(x,x+lp_x)$ and $(z,z+lp_z)$.

(a)

		Fig. 5		Fig. 6		Fig. 7	
		$v=5$ a.u.		$v=1.4142$ a.u.		$v=0.7$ a.u.	
	Z	ϵ	l	ϵ	l	ϵ	l
a	-3	0.03	0.1	0.02	0.3	0.4	0.3
b	0	0.025	0.1	0.025	0.35	0.6	0.4
c	5	0.045	0.3	0.1	0.6	1.5	1.5
d	500	2.5	30	4	40	35	100

(b)

		Fig. 8		Fig. 9	
		$v=1.4142$ a.u.		$v=0.7$ a.u.	
	Z	ϵ	l	ϵ	l
a	-3	0.02	0.3	0.16	0.3
b	0	0.03	0.35	0.2	0.4
c	5	0.08	0.6	1	1.5
d	500	3.5	40	22	100

C. Arrow diagrams and momentum densities

In this paper, our basic tool to illustrate the mechanisms will be $\{\mathbf{r},\mathbf{p}\}$ arrow diagrams, introduced in Ref. [2], and displaying the positions and momenta of ionizing electrons that are located near the collision plane. Specifically, for fixed values of the internuclear coordinate $Z=\mathbf{R}\cdot\hat{\mathbf{v}}=vt$ along a given nuclear trajectory, each diagram consists of a set of arrows drawn from the electron (x,z) coordinates to the head values $(x+lp_x,z+lp_z)$. The x, z, p_x, and p_z data are the spatial and momentum coordinates, with respect to the target nucleus which is at rest, of the ionizing electrons that lie at the time $t=Z/v$ within the slab $-\varepsilon<y<\varepsilon$ about the collision XZ plane; this half-width ε was varied whenever necessary to study the mechanisms. In Table I we give the values of ε used in our drawings, as well as those of the scaling factor l for the arrows. For a meaningful comparison of the diagrams, the l values were chosen to be the same for microcanonical and hydrogenic calculations, whereas different values of ε were required to optimize visualization. It should be taken into account that not all electrons appearing in the diagrams at different times are necessarily the same, because as $Z=vt$ increases, some particles, with sizable p_y values, depart from the slab region, while the larger ε values employed result in that some other electrons, with smaller p_y values, are then included.

Unlike Ref. [2], our present illustrations display separate arrow diagrams corresponding to the molecular-type ρ^i_- and nonmolecular ρ^i_+ ionizing distributions, defined in Sec. II B. Furthermore, to bring forth any relation between the distribution of molecular-type ionizing electrons and the shape of the potential-energy surface $V(\mathbf{r})=-1/r-2/|\mathbf{r}-\mathbf{R}|$, we superposed some lines of force (which are parallel to ∇V and perpendicular to the equipotential curves) onto the arrow diagrams for the distribution ρ^i_- and for $Z=5500$ bohr. For the sake of clarity, the lines of force are excluded from other diagrams, and from the regions closest to the nuclei.

In this work spatial densities will not be presented, for conciseness. On the other hand, illustrating the momentum distributions is indispensable for a quantitative analysis of the arrow diagrams. However, it is sufficient for our purposes to display the densities $\rho(p_z)$ projected along the laboratory-fixed $\hat{\mathbf{p}}_z=\hat{\mathbf{Z}}=\hat{\mathbf{v}}$ direction: we have integrated the ionizing distribution $\rho^i(\mathbf{r},\mathbf{p};v,b,t)$ over the spatial and p_x,p_y coordinates, thereby obtaining

$$\rho^i(p_z;v,b,t)=\int d\mathbf{r}\int dp_x\int dp_y\rho^i(\mathbf{r},\mathbf{p};v,b,t). \quad (6)$$

By further taking $\hat{\mathbf{X}}=\hat{\mathbf{b}}$, the Y axis is always perpendicular to the collision plane, in this reference frame.

III. RESULTS AND DISCUSSION

A. Ionization cross sections

In Ref. [2] we displayed results for the ionization cross section σ^i, obtained from CTMC calculations, and an initial microcanonical distribution (1), for the energy range 12 keV amu$^{-1}\leqslant E\leqslant$10 MeV amu^{-1} (nuclear velocities 0.7 a.u.$\leqslant v\leqslant$20 a.u.). We showed that the method yields good agreement with experiment for $v\geqslant 2$ a.u., whereas for $v<2$ a.u. one obtains a shift of the threshold rise. This liability is offset when the initial hydrogenic distribution (2) is employed. This was shown in Ref. [14], and is confirmed in Fig. 1 down to $v=0.5$ a.u. Besides the data from Ref. [14], we also include the results of Refs. [25,26], the close-coupling values of Refs. [27,28], [29], [30] and [3]; and the measurements of Refs. [31,32]. Near threshold, the improvement reached with the hydrogenic CTMC method is seen to be sufficiently good for the present purposes; on the other hand, for 2 a.u.$\leqslant v\leqslant$4 a.u. the microcanonical cross sections are closer to the experiment (see, however, remarks on the measured data in Ref. [30]), and, for $v>4$ a.u., our microcanonical and hidrogenic cross sections coincide. Incidentally, the small differences between our data and those of Refs. [25,26,14] are probably due to our improved statistics.

We showed in Ref. [2] that the improvement obtained with the hydrogenic distribution also held for the probabilities, insofar as one could tell from accurate results that were available to compare with the classical ones. For the sake of conciseness, we do not complement this here by showing the agreement between our hydrogenic ionization probabilities and the corresponding (unpublished) data of the calculations reported in Ref. [3]. We conclude that the inaccuracy of the microcanonical results at low v is mostly due to the abrupt decrease of the corresponding initial spatial density with r, and not to the use of the classical method. As also shown in Ref. [2], from the contribution $bP(b)$ of the ionization probabilities $P(b)$ to the cross section, nuclear trajectories with $b=2$ bohr can be considered sufficiently representative, and we shall take this choice in our present illustrations.

It should be stressed that, in the same spirit of Refs. [13,2,3], our following discussion refers to the *dominant* features of the ionization mechanism. As is well known (see, e.g., the reviews quoted in Sec. I), subdominant processes, such as the capture-to-the-continuum peak, and the binary encounter maximum at high v, are also very important from

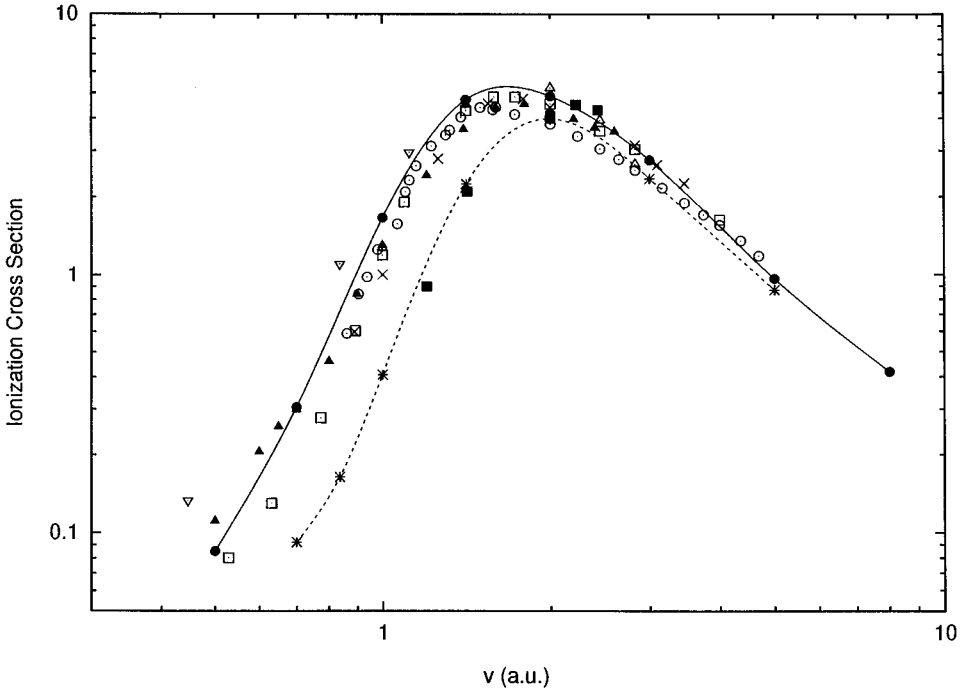

FIG. 1. Ionization cross section in $He^{2+}+H$ collisions (10^{-16} cm^2) as a function of relative nuclear velocity v: (●) present work using an initial hydrogenic distribution; (★) present work using an initial microcanonical distribution; (⊙) experimental data of Refs. [31,32]; (■) results of Refs. [25,26]; (△) Hardie and Olson [14]; (▽) Winter [27,28]; (full triangle) Errea *et al.* [3]; (×) Kuang and Lin [30]; and (□) Toshima [29].

the point of view of interpreting double-differential cross sections, and require much better statistics.

B. Ionization results using a microcanonical initial distribution

For the representative trajectories with impact parameter $b=2$ bohr and nuclear velocities $v=5$, 1.4142, and 0.7 a.u. in Figs. 2(a1) and 2(a2), 3(a1) and 3(a2), and 4(a1) and 4(a2), respectively, we illustrate the arrow diagrams (see Sec. II B) displaying the positions and momenta of ionizing electrons lying in a slab $-\varepsilon<y<\varepsilon$ about the x,z collision plane. In a vertical layout, the figures illustrate the time variation of the ionizing distributions. We have selected the internuclear distances $Z=vt=-3$ bohr ($\alpha=a$), 0 bohr ($\alpha=b$), 5 bohr ($\alpha=c$), and 500 bohr ($\alpha=d$), along the representative nuclear trajectories with impact parameter $b=2$ bohr. The evolution of the nonmolecular distribution ρ^i_+ is shown on the left ($\beta=1$) of each figure, and that of the molecular-type distribution ρ^i_- on the right ($\beta=2$). It should be recalled that the drawings exclusively refer to the ionizing electrons, and therefore the elastic, excitation and capture clouds are not shown. To complement the diagrams, Fig. 5 displays the corresponding longitudinal densities $\rho^i(p_z)$.

A global consideration of the figures shows that, roughly speaking, the dominant classical mechanism giving rise to ionization for the energy range considered is as follows. The first step [exemplified by the distance $Z=-3$ bohr in Figs. 2(a2), 3(a2) and 4(a2)] is a shift of the electron cloud towards the projectile [33], due to Coulomb attraction. As may be expected, since the structure of the polarized cloud is still of atomic character, and atomic-type electrons are but a particular case of molecular-type electrons, most of the drifting particles still have a molecular energy $E_m<0$; consequently, we obtain $\rho^i\approx\rho^i_-$. For $Z>-3$ bohr, the next steps of the ionization mechanism strongly depend on the projectile velocity.

When the relative nuclear velocity v is larger than that of the cross-section maximum (as in the situation exemplified in Fig. 2, for $v=5$ a.u.), the projectiles goes so fast with respect to the target electron that capture is a secondary process, and most polarized electrons are left behind in either an excited, bound state of the target, or an ionizing state. In particular, due to the pull from the projectile, a part of the cloud picks up enough energy so that it eventually ionizes. It is remarkable that the portion of this ionizing cloud that is close to the target still preserves, at small internuclear distances, a molecular character: for instance, we see from Fig. 2(b2) for the velocity $v=5$ a.u., that about half of the ionizing electrons are described by ρ^i_-, while the rest of the distribution ρ^i_+ of Fig. 2(b1) lies closer to the projectile. As the nuclei separate, the nonmolecular part increases at the expense of the molecular one, and at large internuclear distances [$Z=500$ bohr in Figs. 2(d1) and 2(d2)] the $\rho^i_-\rightarrow\rho^i_+$ passage is practically complete, and consequently the whole ionizing cloud is nonmolecular. In this asymptotic region, most of the ionizing electrons have momenta $|p_z|<v$ that are close to the target velocity (equal to 0 in our reference frame). This is confirmed in Fig. 5, and shows that at large nuclear velocities the longitudinal momentum density function tends to the well-known soft electron maximum in the high-energy direct ionization mechanism.

In the other extreme (see, e.g., Fig. 4 for $v=0.7$ a.u.), for $v<1$ a.u. the drifting process mainly causes electron transfer. However, we see from Figs. 4(a2) and 4(b2) (for $v=0.7$ a.u.) how a relatively small number of the polarized

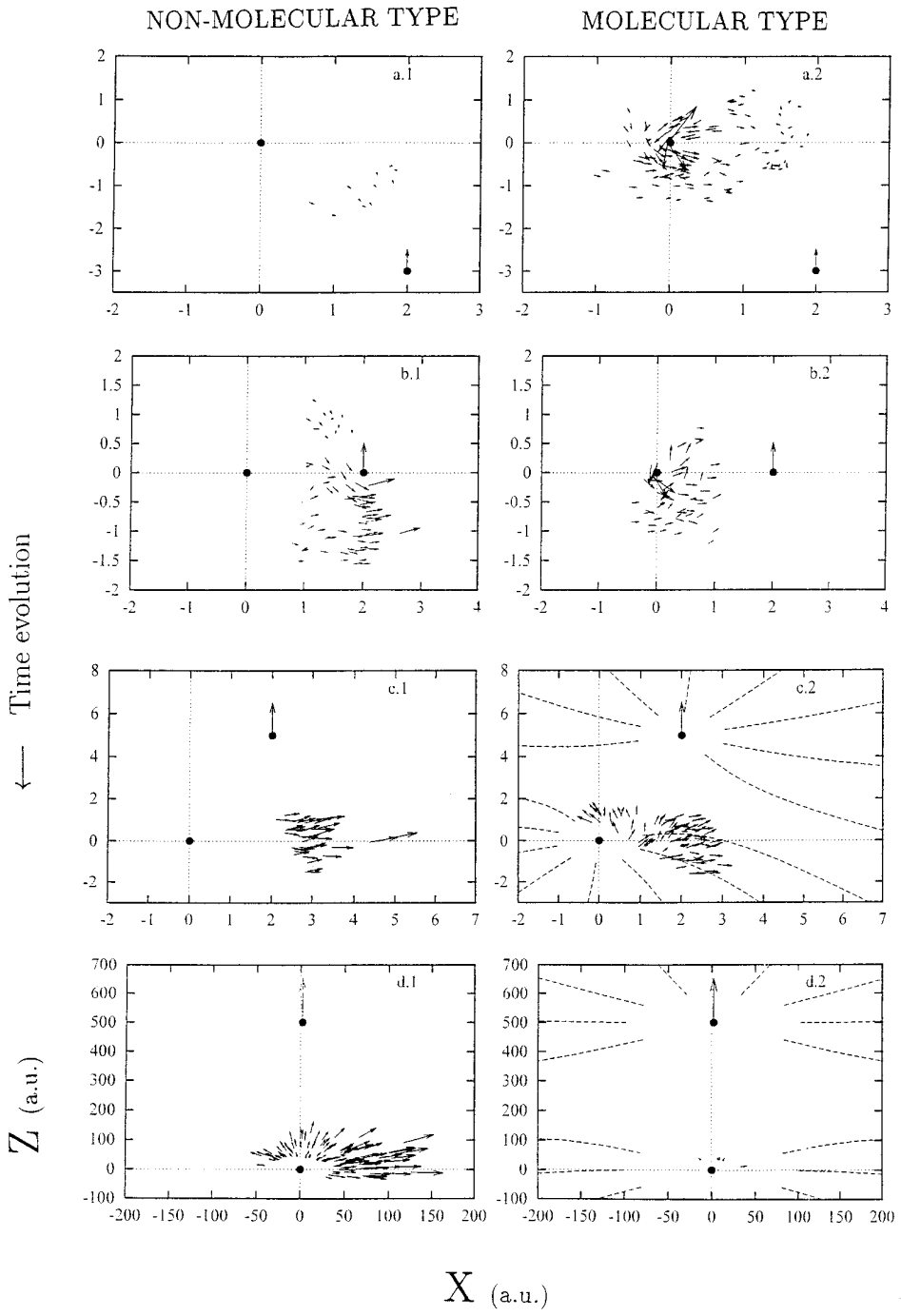

FIG. 2. Arrow diagrams for a microcanonical calculation displaying the position and momentum of ionizing electrons lying in the slab $-\varepsilon<y<\varepsilon$ bohr about the collision plane for (a) $Z=-3$ bohr, (b) $Z=0$ bohr, (c) $Z=5$ bohr, and (d) $Z=500$ bohr. (1) $E_m>0$ and (2) $E_m<0$. The figures describe the time evolution of nonmolecular and molecular distributions for $v=5$ a.u. as one goes down. The momenta are defined with respect to the target, and the nuclear positions are indicated (●). The projectile-velocity vector is also displayed. To show the connection between the distribution and the saddle potential, some lines of force are drawn. The length of the arrows are multiplied by a scaling factor l in order to improve the clarity of the figure (see Table I).

electrons rotate too fast, just miss being captured by the projectile, and are subsequently caught instead by the combined field of the nuclei in Fig. 4(c2). Since most of this molecular-type density stays on top of the saddle region of the potential [see Figs. 4(c2) and 4(d2)] as the nuclei separate, adapting to the shape of the potential surface, this ''surfing'' mechanism [34] may be properly qualified as saddle point type [incidentally, this situation should be contrasted to that of Fig. 2(c2) for $v=5$ a.u., where because of the high speed of the projectile the ''surfing'' is so severely distorted toward the target that the mechanism is not saddle point type].

As the collision proceeds, we again have a $\rho_-^i \rightarrow \rho_+^i$ transition, which takes place at Z values that are larger the smaller the value of v: for example, even at such a large distance as $Z=500$ bohr, we have for $v=0.7$ a.u. and $b=2$ bohr that the distribution ρ_+^i only accounts for about

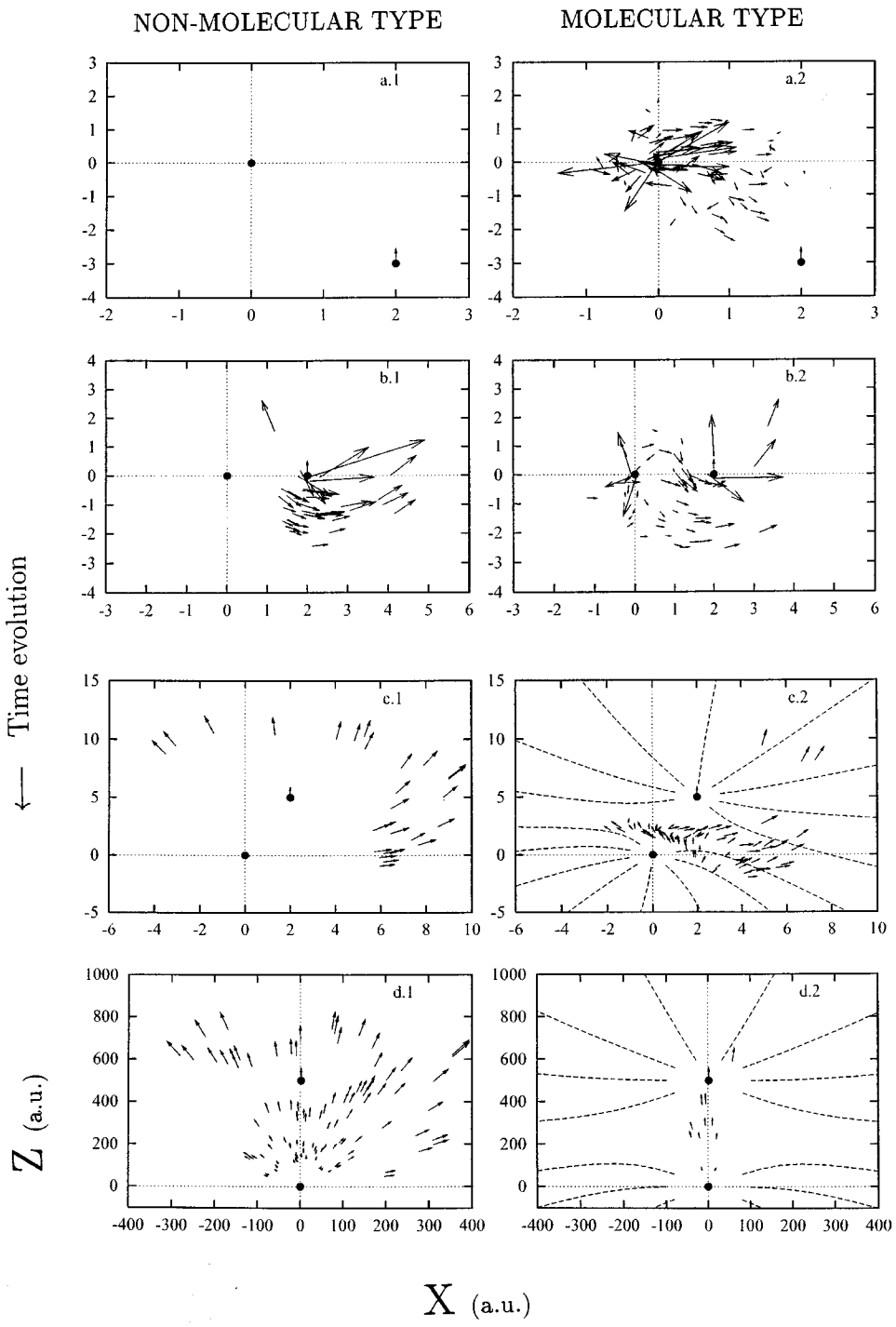

FIG. 3. Same as Fig. 2 for $v=1.4142$ a.u.

25% of the ionizing trajectories. Moreover, while ρ^{i}_{-} is concentrated about the x,z collision plane in the y direction, the nonmolecular density ρ^{i}_{+} extends over larger y domains. A consequence of the latter, together with the different values of $\varepsilon=1.5$ and 35 bohr (see Table I), employed in the diagrams for $Z=5$ and 500 bohr, respectively, result in that some nonmolecular electrons appear in Fig. 4(d1), whereas they are absent from Fig. 4(c1).

This illustration of the saddle-point character of molecular-type ionizing electrons at $v=0.7$ a.u. is complemented by Fig. 5. We see in this figure that the behavior of $\rho(p_z)$ is markedly different from that for $v>1$ a.u., and thus from that explained in Ref. [2]. First, at $Z=0$, and because of its interaction with the slow projectile, the drifting cloud displays a broad $\rho(p_z)$ density with the principal maximum close to $p_z=v$. Second, at $Z=5$ a.u. a sizable amount of electrons that are trapped by the saddle part of the potential run quasiparallel to the lines of force and quasi-perpendicular to v [see Fig. 4(c2)], accordingly, $\rho(p_z)$ becomes peaked at $v=0$. Third, at large Z, and because of a post-collision interaction with the combined nuclear field, $\rho(p_z)$ ends up with a maximum at the center of force value $p_z=(1+\sqrt{2})^{-1}v\approx 0.3$ a.u.. Hence the existence of SPI as a separate ionization mechanism at low v is definitely demonstrated.

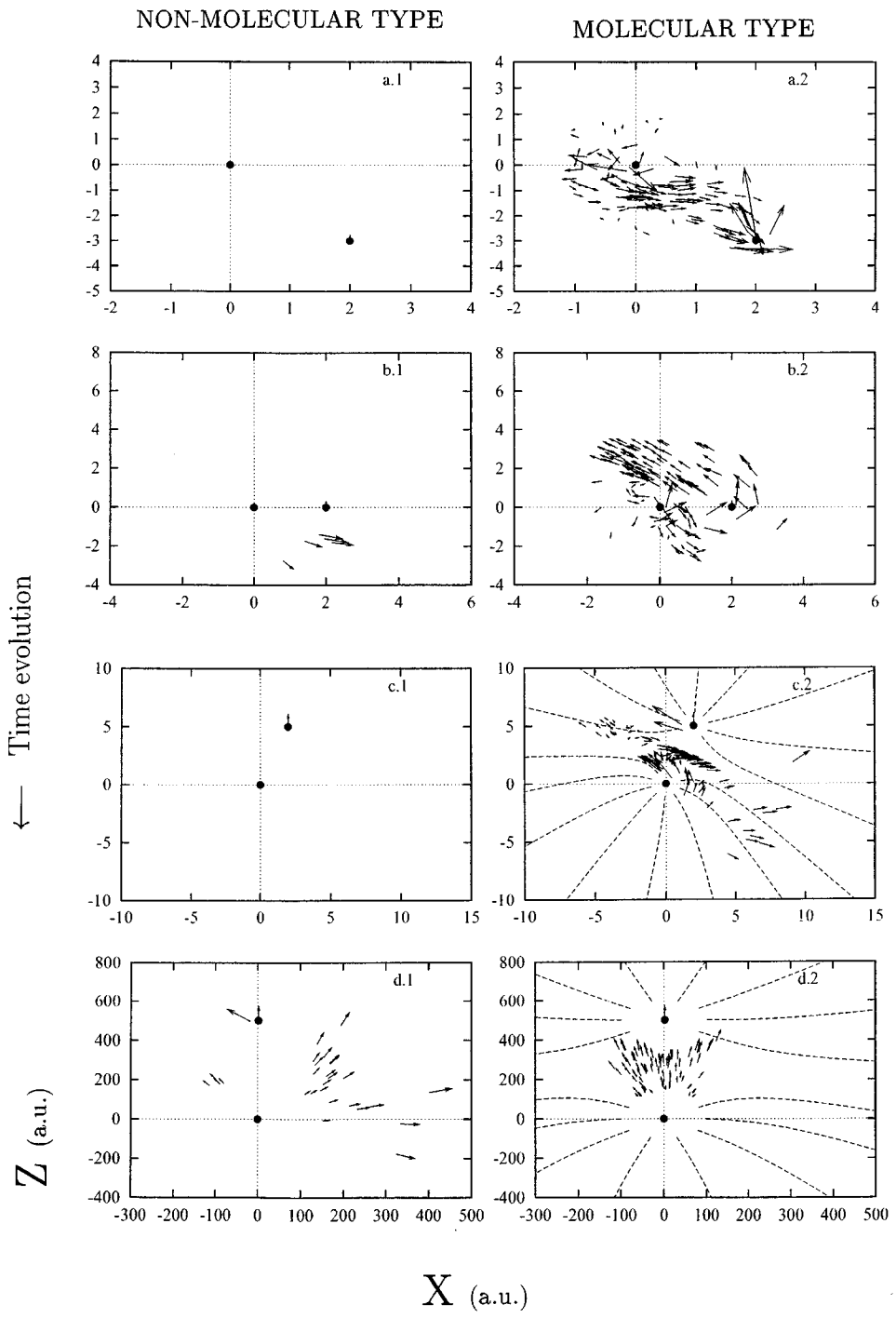

FIG. 4. Same as Fig. 2 for $v = 0.7$ a.u.

As stressed in Ref. [2], the situation for velocities close to the cross-section maximum is interesting, because it permits one to understand the evolution from lower to higher nuclear velocities, and because stronger interactions take place. We now show how the separate time evolutions of ρ^i_- and ρ^i_+ permit one to explain some features mentioned in our previous work for $v = 1.4142$ a.u.

Starting with ρ^i_-, we see that its time variation in Fig. 3 is intermediate between those of Figs. 2 and 4. In addition, it shows that the peak of $\rho(p_z)$ at approximately the center of force value, which appears in Fig. 5 for $v = 1.4142$ a.u. and $Z = 5$ bohr, is accompanied by a close relation between the structure of ρ^i_- in Fig. 3(c2) and the shape of the saddle region of the potential. The peak disappears at large internuclear separations, and our diagrams illustrate that this is due to the fact that most of the electrons making up ρ^i_- at $Z = 5$ bohr [Fig. 3(c2)] are less efficiently trapped by the saddle region of the nuclear potential, and become nonmolecular at $Z = 500$ bohr [see Fig. 3(d1)]: at this distance ρ^i_- only accounts for about 10% of ionization.

Turning now to ρ^i_+, a new feature at intermediate velocities [2] is that a sizable part of the ionizing cloud collides with either nuclei, and thereby becomes nonmolecular. This is illustrated in Figs. 3(b1), 3(a2) and 3(b2). Only some of

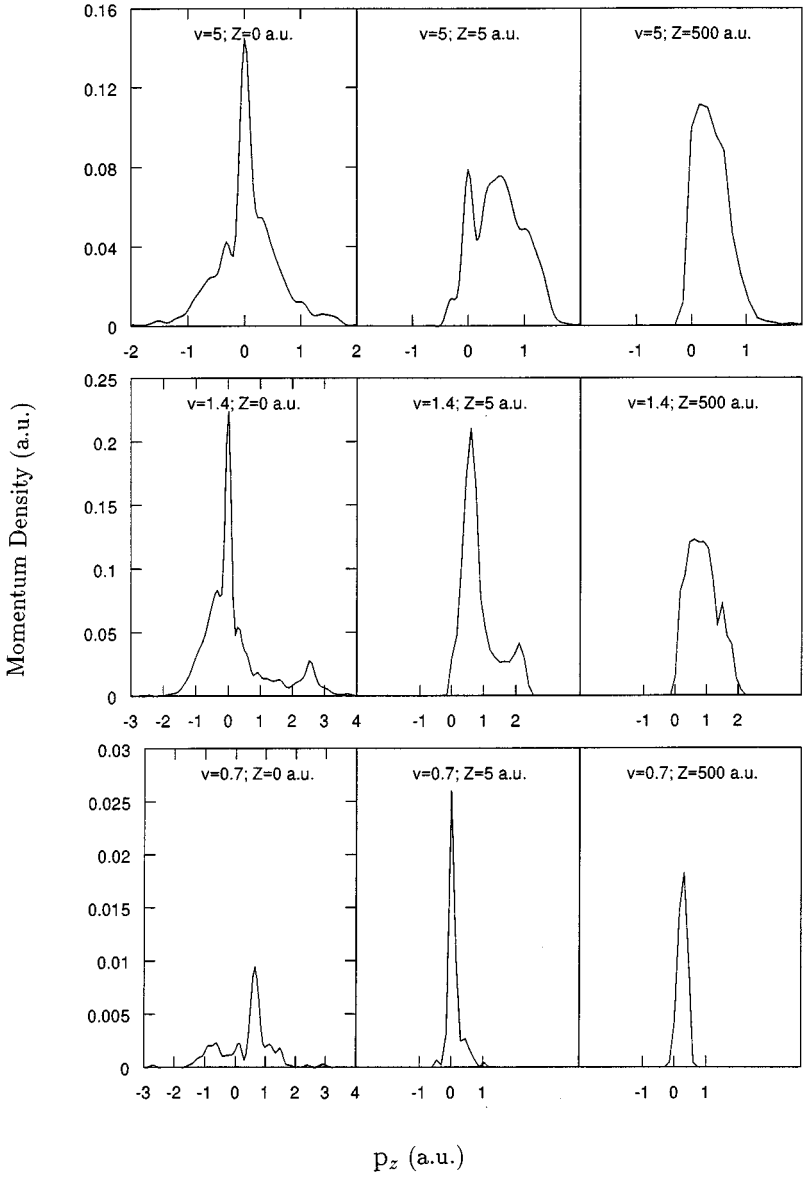

FIG. 5. Momentum densities $\rho^i(p_z)$ in the **v** direction for a microcanonical calculation at $Z=0$, 5, and 500 bohr. $v=5$ a.u. (up), $v=1.4142$ a.u. (middle), and $v=0.7$ a.u. (down).

these electrons, which have small $|p_y|$ values, lie close to the collision plane, and therefore appear in the diagrams of Figs. 3(c1) and 3(d1). In particular, these figures show that, as a result of hard encounters with the projectile, there arises an asymmetric shell of ionizing electrons in the **v** direction. The intersection of the shell with the $[-\varepsilon,\varepsilon]$ slab is a crescent, formed by nonmolecular electrons with velocities $p_z \approx 2v$ for $Z=5$ bohr, and $p_z \approx v$ for $Z=500$ bohr (see secondary peaks in the momentum density of Fig. 5). Hard collisions with the target produce a more isotropic distribution.

C. Ionization results using a hydrogenic initial distribution

Since a comparison between the CTMC results using initial microcanonical and hydrogenic electron distributions shows that the dominant ionization mechanism is qualitatively the same, our discussion will focus on the main differences, while also illustrating the similarities. Furthermore, since these differences appear at low v, the arrow diagrams will only be given for $v=1.4142$ and 0.7 a.u. in Figs. 6 and 7, respectively, for the same representative trajectories with $b=2$ bohr as in Sec. III B; the corresponding momentum distributions are displayed in Fig. 8.

As may be expected, the most important novelties when the initial distribution of Eq. (2) is employed stem from the more spread initial spatial density, resulting in a stronger polarization of the electronic cloud. Three consequences are that collisions with larger impact parameters become ionizing; there appear a larger number of hard encounters with the nuclei at lower impact energies; and we obtain a smoother transition between the processes described in Sec. III B.

We start with the nuclear velocity $v=1.4142$ case (Fig. 6), for which the arrow diagrams are similar to those of Fig. 3 described in Sec. III B. Nevertheless, and because of the stronger polarization of the electron cloud, now hard encoun-

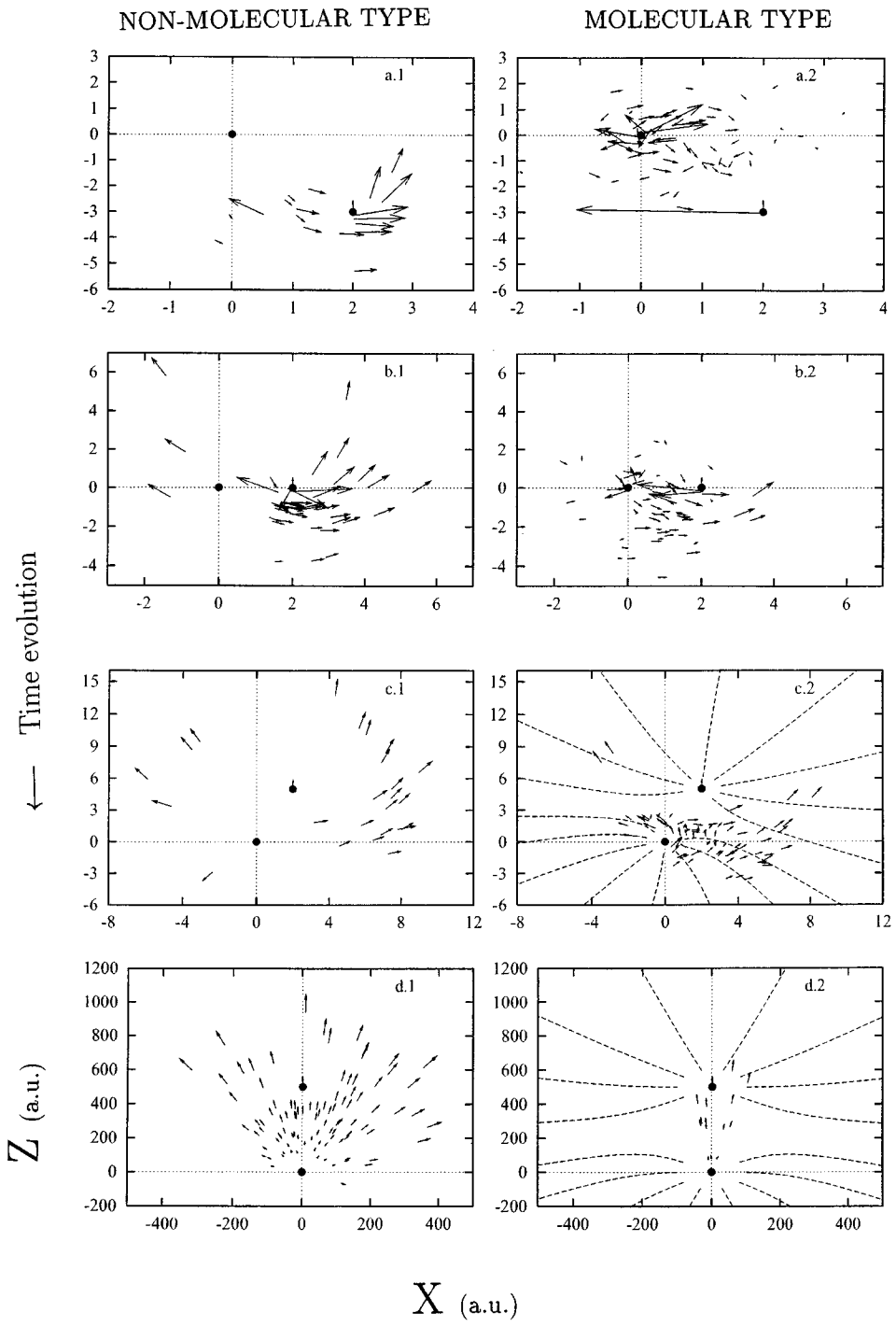

FIG. 6. Same as Fig. 2 for a hydrogenic calculation for $v = 1.4142$ a.u.

ters with the projectile take place sooner [see Fig. 6(a1), to be contrasted with the empty diagram for ρ^i_+ in Fig. 3(a1)]. Another difference, which may be observed in Fig. 6(c2) for $Z = 5$ bohr, is that the ρ^i_- density is more spread in the saddle region of the potential than in Fig. 3(c2). Also, the secondary peak found in $\rho^i(p_z)$ at $p_z \approx 2v$ in Fig. 5 (for $v = 1.4142$ a.u.) is less conspicuous in Fig. 8 for the hydrogenic case. Finally, the asymptotic distribution [see Fig. 6(d1)] displays a less clear-cut spatial boundary between molecular and (crescent) nonmolecular electrons than in Fig. 3(d1), and the final momentum distribution function now has a single, broad maximum in Fig. 8. Consequently, the (approximately) sharp classification between three ionizing mechanisms made in Ref. [2] for $v = 1.4142$ a.u. is seen not to be a general feature, and to be due to the use of an initial spatial density that was too compact.

The differences between hydrogenic and microcanonical distributions become more conspicuous at lower velocities. For example, at $v = 0.7$ a.u. and $Z = 5$ bohr, changes in Fig. 7 with respect to Fig. 4 are substantial; notice in this respect the smaller values of ε employed in the former. In particular, we have an enhancement of the hard encounter mechanism

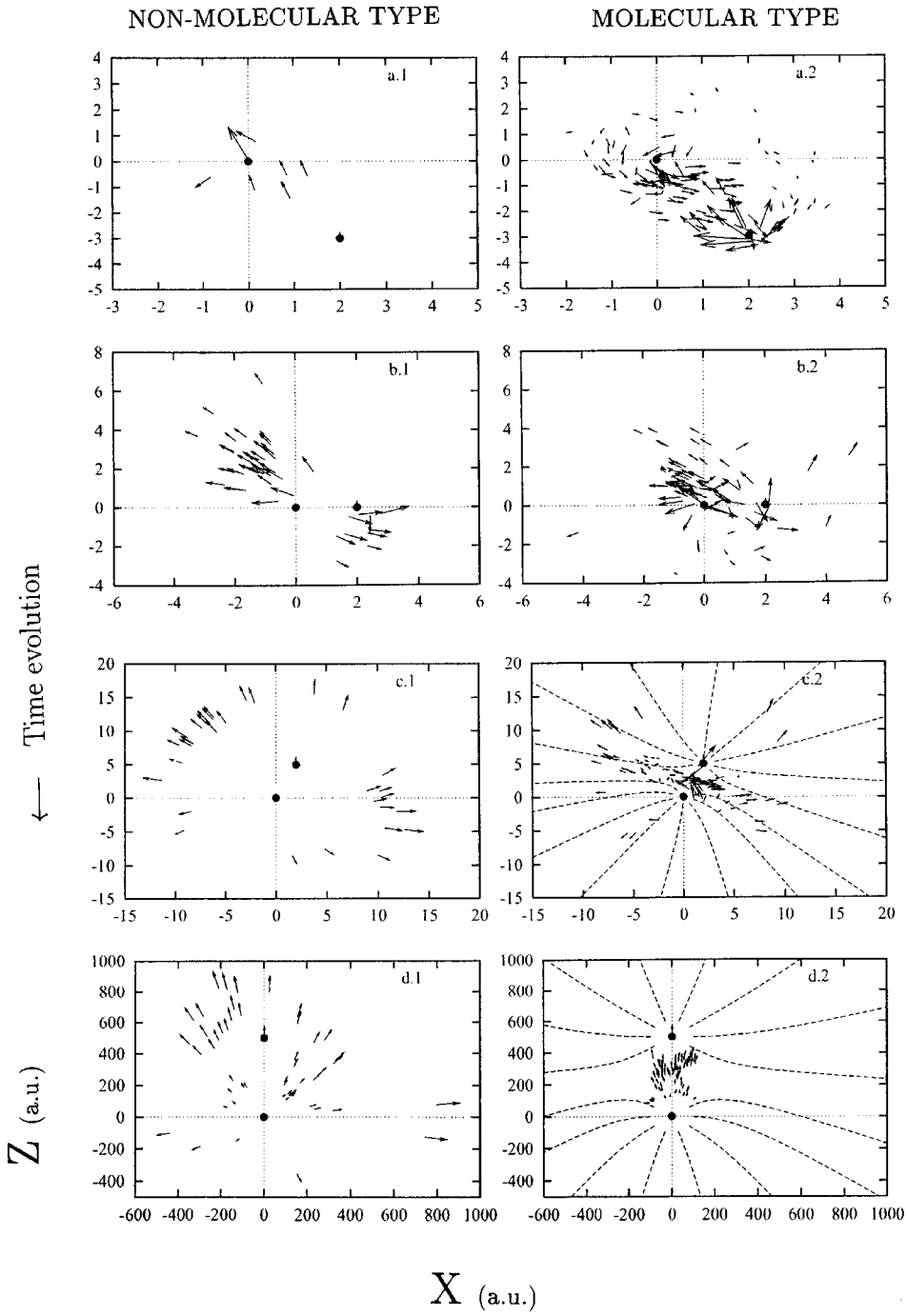

FIG. 7. Same as Fig. 6 for $v = 0.7$ a.u.

(with the target nucleus and the projectile). One consequence is that the crescent due to the electron-projectile collisions is clearly visible in Figs. 7(c1) and 7(d1), whereas it is practically absent in Figs. 4(c1) or 4(d1).

A consequence of these differences is that at $v = 0.7$ a.u. the ionization mechanism obtained in the hydrogenic calculations is a little less molecular type than for the microcanonical ones. Accordingly, in order to obtain $\rho^i \approx \rho^i_-$ at short R with the former method, one has to treat lower velocities than with the latter. A similar feature concerns SPI: it is apparent in Fig. 7(c2) that molecular-type electrons are less efficiently trapped by the saddle potential, and accordingly have a higher probability to escape from it than in Fig. 4(c2). A consequence is that at $R = 500$ bohr and for the trajectory considered, the proportion of molecular electrons is 68%, a little lower than for the microcanonical distribution (75%).

Notwithstanding these differences, the most important result is that the main conclusions from the microcanonical calculations are unchanged when a more accurate initial representation is employed. In agreement with our findings of Sec. III B, Fig. 7 shows that, as one approaches threshold, an increasing proportion of ionizing electrons are molecular type, and from these an increasing number are trapped in the saddle region of the potential and have an asymptotic mo-

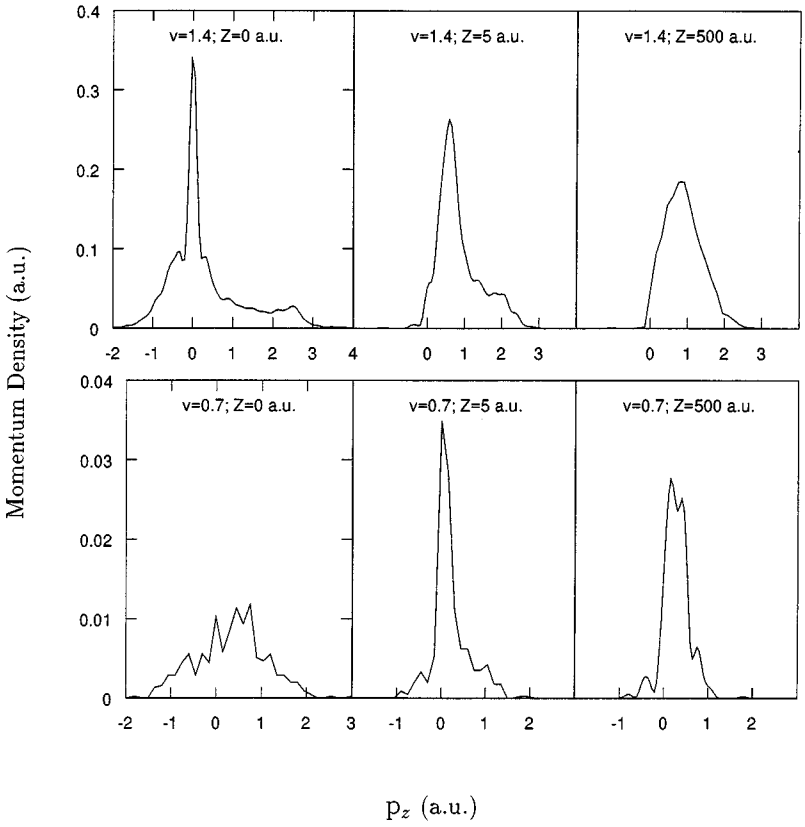

FIG. 8. Momentum densities $\rho^i(p_z)$ in the **v** direction for a hydrogenic calculation for $Z=0$, 5, and 500 bohr. $v=1.4142$ a.u. (up) and $v=0.7$ a.u. (down).

mentum density peaked about the center of force value, because of a postcollision interaction: see Fig. 8 for $v=0.7$ a.u. Therefore, we conclude that the appearance of SPI at low collisional energies is not an artifact due to the use of a microcanonical initial electronic distribution, and also arises for treatments that yield accurate cross sections in that energy region.

IV. CONCLUSIONS

From a study of the separate time evolutions of molecular-type and nonmolecular ionizing distributions for the benchmark case of $He^{2+}+H(1s)$ collisions, we conclude that (i) at sufficiently low nuclear velocities, the ionization mechanism is determined by the molecular-type distributions; (ii) at these velocities, it may also be properly qualified as saddle-point ionization; (iii) these features hold for CTMC calculations starting from either a microcanonical distribution or the improved one of Eq. (2) that provides a better representation of the spatial $H(1s)$ cloud; (iv) and SPI and direct ionization are the low- and high-v limits of a common process involving molecular-type electrons at short internuclear distances.

More specifically, with respect to the first three conclusions, when the relative nuclear velocity is much lower than that of the cross section maximum, the main steps of the ionization mechanism are as follows. One part of the polarized electron cloud, given by the molecular-type distribution ρ^i_-, misses being captured by the projectile, and is caught at short R by the combined nuclear potential. For $t>0$, the shape of ρ^i_- is determined by the form of the saddle part of this potential; furthermore, in the asymptotic region its longitudinal momentum density $\rho(p_z)$ becomes peaked about the center of the nuclear force value because of a postcollision interaction. We have concluded that the name SPI fitly describes such a mechanism.

The best way to portray conclusion (iv) above regarding the higher-v results is to compare the variation in Figs. 4(c2)→4(d2), to that in Figs. 2(c2)→2(d1): the mechanism is clearly analogous, though dissimilar: at higher collision energies the role of the center of nuclear force has waned (no SPI), and the electrons have become nonmolecular in a faster way. Furthermore, a consideration of the outcome in both cases shows that as the impact energy increases, the SPI mechanism at low energies [Fig. 4(d2)] is replaced by a direct ionization [Fig. 2(d1)] mechanism in which most electrons depart with momenta $p_z\approx 0$. In addition, at impact energies near the maximum of the ionization cross section, we have a more complex situation, because of a sizable number of hard encounters with target and projectile nuclei.

Finally, some comments on the picture of molecular-type ionization that emerges from our diagrams may be relevant. In this respect, we notice that the electrons making up ρ^i_- have been called molecular type because they are bound in a Born-Oppenheimer clamped nuclei frame, and not because

they circle round both nuclei in a boundlike motion (which we have seen is not the case). Keeping this difference in mind, we have that, at short R, and for all nuclear velocities treated here, several important steps of the ionization process can be said to have molecular characteristics: the polarization effect, the SPI mechanism at low v, and a sizable part of the direct ionization mechanism at higher v, are all of molecular type. The role of molecular-type ionizing electrons is the more prominent the lower the impact energy, and may be taken as a justification of the success of molecular treatments of ionization, such as the hidden-crossing [15,16] and close-coupling [4,1] approaches.

On the other hand, it is also important to realize that a sizable portion of the ionizing distribution has a nonmolecular character. In particular, all ionizing densities eventually become nonmolecular, and the $\rho^i_- \rightarrow \rho^i_+$ transition occurs the sooner the nuclear velocity becomes larger.

ACKNOWLEDGMENTS

This work was partially supported by DGICYT Project No. PB93-0288-C02, and by the project ENRESA (Generac.resid.activ.neutronica.react.fus. Cod. 0703240).

[1] C. Harel, H. Jouin, B. Pons, L. F. Errea, L. Méndez, and A. Riera, Phys. Rev. A **55**, 287 (1997).
[2] C. Illescas, I. Rabadán, and A. Riera, J. Phys. B **30**, 1765 (1997).
[3] L. F. Errea, C. Harel, C. Illescas, H. Jouin, L. Méndez, B. Pons, and A. Riera, in *Proceedings of the XX International Conference on the Physics of Electronic and Atomic Collisions*, edited by H. Winter, G. Betz, and F. Aumayr (Institut für Allgemeine Physik, TU Wein, Vienna, 1997).
[4] L. F. Errea, C. Harel, H. Jouin, L. Méndez, B. Pons, and A. Riera, J. Phys. B **27**, 3603 (1994).
[5] R. E. Olson, Phys. Rev. A **27**, 1871 (1983).
[6] M. McCartney, Phys. Rev. A **52**, 1213 (1995).
[7] P. D. Fainstein, V. H. Ponce, and R. D. Rivarola, J. Phys. B **24**, 3091 (1991).
[8] J. S. Briggs and J. N. Macek, Adv. At. Mol. Phys. **28**, 1 (1991).
[9] B. H. Bransden and M. H. C. McDowell, *Charge Exchange and the Theory of Ion-Atom Collisions* (Oxford Science, Oxford, 1992).
[10] D. Eichenauer, N. Grun, and W. Scheid, J. Phys. B **14**, 3929 (1981).
[11] J. S. Cohen, J. Phys. B **18**, 1759 (1985).
[12] N. Gryziński, J. Phys. B **20**, 4741 (1987).
[13] G. Bandarage and R. Parson, Phys. Rev. A **41**, 5878 (1990).
[14] D. J. W. Hardie and R. E. Olson, J. Phys. B **16**, 1983 (1983).
[15] J. P. Grozdanov and E. A. Solov'ev, Phys. Rev. A **42**, 2703 (1990).
[16] R. K. Janev, G. Ivanovsky, and E. A. Solov'ev, Phys. Rev. A **49**, R645 (1994).
[17] R. Abrines and I. C. Percival, Proc. Phys. Soc. London **88**, 861 (1966).
[18] R. E. Olson and A. Salop, Phys. Rev. A **16**, 531 (1977).
[19] J. S. Burlisch and J. Stoer, Numer. Math. **8**, 1 (1966).
[20] C. O. Reinhold and C. A. Falcón, J. Phys. B **21**, 1829 (1988).
[21] S. B. Schneiderman and A. Russek, Phys. Rev. **181**, 311 (1969).
[22] W. R. Thorson and J. B. Delos, Phys. Rev. A **18**, 117 (1978).
[23] C. Harel and H. Jouin, Europhys. Lett. **11**, 121 (1990).
[24] L. F. Errea, C. Harel, H. Jouin, J. M. Maidagan, L. Méndez, B. Pons, and A. Riera, Phys. Rev. A **46**, 5617 (1992).
[25] R. E. Olson and A. Salop, Phys. Rev. A **16**, 531 (1977).
[26] R. E. Olson, Phys. Rev. A **18**, 2464 (1978).
[27] T. G. Winter, Phys. Rev. A **25**, 697 (1982).
[28] T. G. Winter, Phys. Rev. A **37**, 4656 (1988).
[29] N. Toshima, Phys. Rev. A **50**, 3940 (1994).
[30] J. Kuang and C. D. Lin, J. Phys. B **30**, 101 (1997).
[31] M. B. Shah and H. B. Gilbody, J. Phys. B **14**, 2361 (1981).
[32] M. B. Shah, D. S. Elliot, P. McCallion, and H. B. Gilbody, J. Phys. B **21**, 2455 (1988).
[33] P. L. Grande and G. Schiwietz, J. Phys. B **28**, 425 (1995).
[34] V. D. Irby, Phys. Rev. A **51**, 1713 (1995).